Feasibility of Ice Segregation Location by Acoustic Emission Detection: A Laboratory Test in Gneiss

(Article begins on next page)

01 September 2025

Feasibility of Ice Segregation Location by Acoustic Emission Detection: A Laboratory Test in Gneiss

S. Duca,[1,2]*[†] *C. Occhiena,*[2] *M. Mattone,*[3] *L. Sambuelli*[4] *and C. Scavia*[2]

[1] eni spa, Upstream and Technical Services LAIP, Milan, Italy
[2] Department of Structural, Building and Geotechnical Engineering, Politecnico di Torino, Turin, Italy
[3] Department of Mechanical and Aerospace Engineering, Politecnico di Torino, Turin, Italy
[4] Department of Environment, Land and Infrastructure Engineering, Politecnico di Torino, Turin, Italy

ABSTRACT

Large slope failures in steep alpine bedrock present significant geological hazards. Ice segregation is thought to be one of the mechanisms involved in high-mountain bedrock fracture but has not been reproduced experimentally in hard, intact rock. Here, we report results from a 3 month freezing experiment that aimed to reproduce ice-lens growth at the interface between the active layer and permafrost in a 15 cm cube of hard, intact rock (Arolla gneiss). Monitoring of acoustic emissions (AEs) recorded the propagation of microcracks horizontally through the block, resulting in a continuous and thick macrocrack near the base of the artificial active layer. Microcracking occurred within an approximate temperature range of $-0.5\,°C$ to $-2.7\,°C$, consistent with ice segregation theory. Hypocentres of recorded AE events were concentrated in a 40 mm thick band between depths of 4.5 and 8 cm in the block. The band approximately coincides with the frozen fringe and indicates that ice segregation can induce micro- and macrocracking in gneiss. Copyright © 2014 John Wiley & Sons, Ltd.

KEY WORDS: ice segregation; laboratory test; acoustic emissions; fracturing

INTRODUCTION

Frost weathering in rock results from the progressive growth of microcracks and relatively large pores wedged open by ice growth (Hallet *et al.*, 1991). Diurnal and annual frost cycles control the timing and magnitude of frost weathering, as highlighted by field monitoring. Porous rock samples have been subjected to bidirectional freezing laboratory tests in order to study the onset of fractures containing segregated ice near the permafrost table: the results would seem to imply the development of ice-filled fractures in permafrost bedrock over long timescales (Murton *et al.*, 2001, 2006). This finding, combined with numerical modelling of the thermal regime in permafrost rock slopes, contributes to the prediction of large-scale rockfalls and rock avalanches triggered by permafrost degradation (Matsuoka and Murton, 2008). These authors suggested that future studies of frost weathering should investigate hard, intact

rocks, which form high mountains; this will help to address the question 'Does microgelivation of hard, intact rocks require an extant microcrack system developed by any process or inherited?' (e.g. Whalley *et al.*, 2004). Laboratory freeze-thaw tests have never caused the generation and propagation of new, visible cracks in hard, intact rock; they have only revealed a decrease in ultrasonic velocity or Young's modulus, or a minor increase in porosity (Matsuoka, 1990; Ondrasina *et al.*, 2002; Whalley *et al.*, 2004). Ice segregation theory suggests that cracks in low-porosity rocks such as granite propagate at low temperatures of $-4\,°C$ to $-15\,°C$ (Walder and Hallet, 1985); previous laboratory simulations have been carried out in high-porosity rocks (tuff and chalk) inducing ice segregation at higher temperatures ($> -2\,°C$).

In recent years, theoretical studies and laboratory experiments have investigated the role of ice segregation in intact rocks (Walder and Hallet, 1985; Akagawa and Fukuda, 1991; Murton *et al.*, 2000, 2006; Chen *et al.*, 2003; Saad *et al.*, 2010). Most laboratory studies use intact rock samples with medium (5–20%) to high (>20%) porosity because intact rocks allow the correlation of rock properties with frost sensitivity, and high-porosity rocks are generally

* Correspondence to: S. Duca, eni E&P, Milan, Italy.
E-mail: silvia_duca@libero.it
[†] Present address: eni spa Upstream and Technical Services/ LAIP Dpt.
Via Maritano, 26 - 20097 S. Donato, Milanese (MI) - Italy

more vulnerable to weathering (Matsuoka, 1990). In contrast, many field studies concern weathering of low porosity (<5%) but jointed rocks, which compose most high mountains (Draebing and Krautblatter, 2012).

The present study seeks to verify the operation of ice segregation and resulting crack growth in hard, intact, saturated rock. It reports the results of a laboratory simulation carried out at the Disaster Planning Laboratory, Politecnico di Torino, Turin, Italy, reproducing ice-lens growth at the interface between a simulated active layer and permafrost (Duca, 2013). The main objective is to test if a saturated hard rock specimen macroscopically fractures as a result of the growth and interconnection of microfractures in response to ice segregation. Ice-lens growth was monitored by measuring heave and settlement of the block surface, and the location of active microgelivation was determined by monitoring acoustic emissions (AEs) (Duca, 2013). The application of the AE technique to ice segregation experiments provides a novel and promising methodology that can yield valuable insights into the processes operating in the evolving fracture zone.

VERIFICATION OF ICE SEGREGATION GROWTH IN MICROCRACKS IN HARD, INTACT ROCKS

Testing of ice segregation in hard rocks requires a specific experimental design. Freezing of pore fluid within microcracks in rock involves complex interactions between thermal, hydraulic and mechanical processes. For example, phase changes in pore fluid caused by temperature variations modify the hydraulic regime of the material, which in turn induces mechanical deformation. At the same time, any change in the hydraulic and mechanical conditions feeds back to the thermal processes by way of advection and changes in ice and water contents (Nishimura *et al.*, 2009).

Numerical simulations were performed in order to define the experimental procedure and to evaluate some predictions. First, numerical analyses were carried out using the finite element method (FEM) code ABAQUS to identify those conditions that would maximise frost cracking by thermal expansion in the rock sample (Duca, 2013): through these studies, the temperature interval that should amplify the propagation of saturated microcracks due to freezing was chosen.

Fully coupled thermo-hydro-mechanical simulations were carried out using the FEM code CODE_BRIGHT to predict the timing, scale and depth of potential macrocracks originating perpendicular to the water flow as a result of ice segregation (Duca, 2013). The CODE_BRIGHT numerical model showed that heat transfer and water transport must be essentially unidirectional and steady state in order to induce fracture propagation by slow continuous freezing associated with a temperature distribution constant in time. Based on these studies, it was decided that the test would last at least 3 months. Simulating the upward-freezing experiment, it was possible to identify the thickness of the 'frozen fringe' (i.e. a transition zone where a considerable amount of water

remains unfrozen, although at subfreezing temperature; Miller, 1978). These data were useful to predict the depth of ice-lens growth and to characterise the thermo-physical state of the sample for subsequent acoustic analysis.

Experimental Set-up

The rock sample used in the experiment was Arolla gneiss collected in the Pelline Valley (Aosta Valley, Italy), where it crops out. Its characteristics are listed in Table 1. A 15 cm cubic block of saturated gneiss in which no macrocracks or visible discontinuities were observed was subjected artificially to thermally induced microcracking before the experiment commenced (Duca, 2013).

The gneiss specimen was subjected to two different thermal cycles, at the Department of Analytical Chemistry, Universitá degli Studi di Torino, Turin, Italy, to induce microcracking. During the first thermal treatment, the specimen was heated to 420 °C at a rate of 0.5 °C/min; the maximum temperature was maintained for 18 h. Then, the specimen was cooled at a gradient rate of 0.1 °C/min. During the second thermal treatment, the sample was subjected first to a thermal shock and then to a new thermal cycle. It was placed in an oven at a temperature of 250 °C for 24 h, and then suddenly cooled in cold water. Finally, it was slowly heated in a furnace at ambient pressure to 420 °C at a rate of 0.5 °C/min. The low rate of heating was used to ensure that cracking events result only from the temperature effect and not from thermal gradients across the sample. The maximum temperature was maintained for 5 days. The block was cooled by exposing it directly to the room temperature.

The specimen was saturated by removing air under a vacuum and forcing water into the pores under high pressure. The procedure was carried out with an apparatus specifically constructed. The sample was placed in a container of demineralised water inside a bell jar, and connected to a turbomolecular pump to obtain and maintain a high vacuum. The pressure in the bell jar was sufficiently low for the water to boil and the sample remained in these conditions for 10 h, and subsequently returned to atmospheric pressure.

Figure 1 shows a cross-section of the sample configuration. The sample was placed over a basal cooling plate,

Table 1 Mechanical characteristics of thermally microcracked Arolla gneiss.

Mechanical characteristics	
ρ [kg/m^3]	2759
φ *[−]	0.15
C_0 [MPa]	106
E_t [GPa]	111
v [−]	0.02
σ_t [MPa]	3

ρ = Density; φ* = porosity; C_0 = uniaxial compressive strength; E_t = tangent Young modulus; v = Poisson's ratio; σ_t = tensile strength.

S. Duca *et al.*

specifically designed and assembled by TE Technology (model CP-121 (Michigan, USA)), and collocated in a box with the sides thermally insulated (Figure 2a–c). The sides of the sample were sealed with silicone to prevent water loss (Figure 3f). A linear temperature gradient with depth of the sample was induced. The thermal regime was determined through the cooling plate controller and an infrared heater installed at a distance of 20 cm from the top surface (Figure 2e). The temperatures of the lower and upper surfaces were set to -12 °C and 5 °C, respectively, based on the results from the FEM ABAQUS model.

The temperature profile was monitored during the test with eight Pt100 platinum resistance thermometers (TC Direct, Turin, Italy) (accuracy 0.02% L 0.1 °C). These were glued with X60 two-component fast-curing adhesive (HBM, Darmstadt, Germany) on one side of the specimen at depths of 1.5, 3, 4.5, 6, 8, 10, 12 and 14 cm (Figure 2d) and then covered by a thermal compound (Artic Cooling MX2, ARCTIC Switzerland AG). The upper surface temperature was periodically measured with an infrared thermometer (model TESTO (Testo, Inc., Sparta, NJ, USA) 830-T1, accuracy 0.1 °C).

An array of eight physical acoustic AE sensors (model NANO30 FN 54–61, Mistras Corporation, Princeton Jct, NJ, USA) counted and determined the approximate location and amplitude of microfracture events (Figure 3a, b). A rigid plexiglass cladding was placed around the gneiss block in order
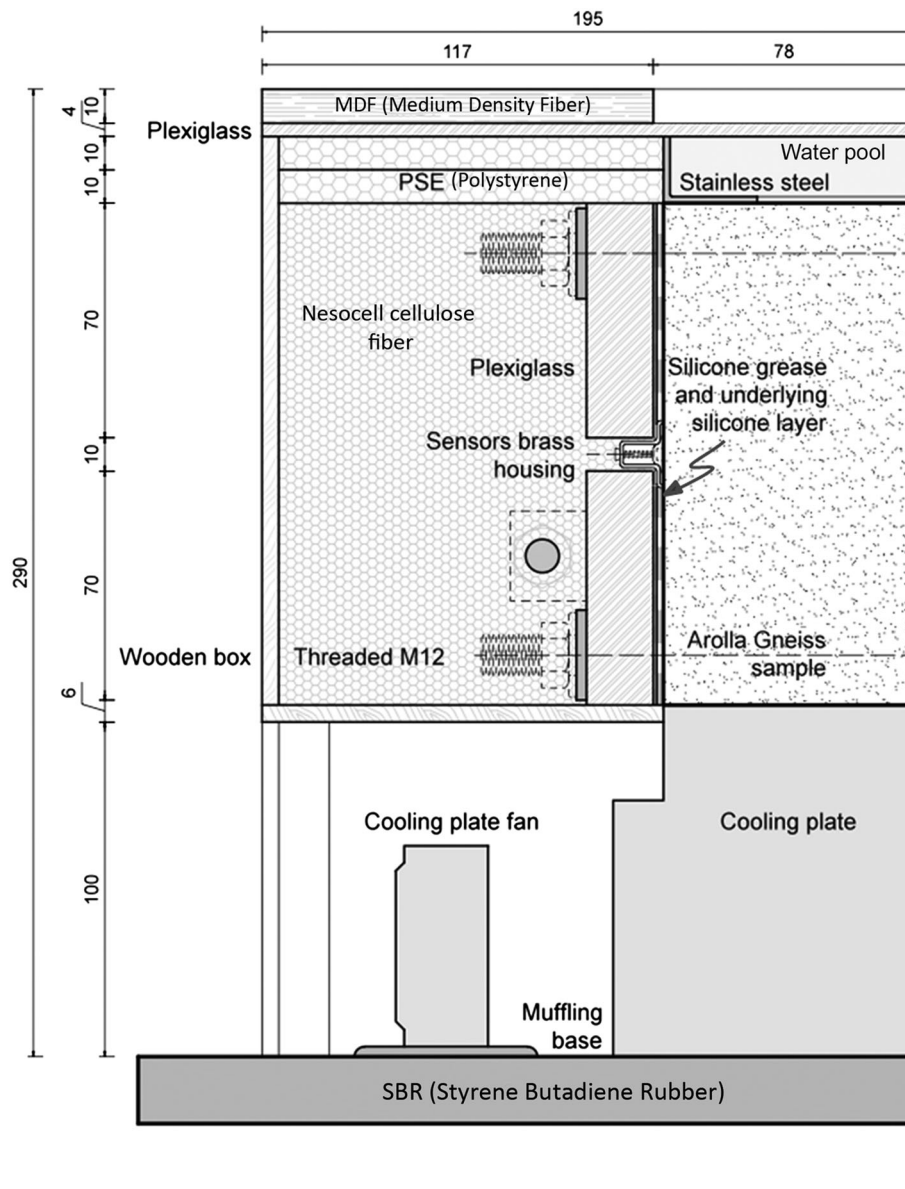

Figure 1   Vertical cross-section of half of the apparatus and the sample configuration (dimensions in mm).

Figure 2 Experimental set-up: (a) sample of cellulose fibre provided by Nesocell (Turin, Italy); (b) cellulose fibre compacted in the wooden box; (c) stainless-steel quadratic pool glued on the top of the block; (d) Pt100 platinum resistance thermometers glued to one side of the block with X60 two-component fast-curing adhesive and then covered by a thermal compound; (e) transparent plexiglass, medium-density fibre sheets and infrared lamp installation.

to ensure that the sensors remained attached to the sample surface (Figure 3c–e). Each AE sensor was connected to a charge amplifier (gain 40 dB, bandwidth 50 kHz–30 MHz) and the signals recorded by a general purpose data acquisition board (Graphtec GL1000, Graphtec Corporation, Japan). The importance of the correct receiver array distribution and details of the adopted solution for the experimental design are discussed by Duca *et al.* (2014). The location of the AE sensors on the sample is shown in Figure 4.

The water content of the rock sample was maintained during the experiment by a 1 cm water head on the top of the specimen.

The top of the box was filled with 20 mm thick polystyrene sheets, and the entire apparatus was covered by a transparent plexiglass sheet to avoid evaporation of water.

MONITORING OF MICROGELIVATION ACTIVITY USING AES

Conventional measures of frost damage provide limited information about the magnitude, timing and location of frost-induced deterioration (Hallet *et al.*, 1991), whereas AEs associated with grain scale fracture can reveal the spatial and temporal distribution of damage (King *et al.*, 2011).

The initiation and growth of microcracks in rock suddenly release energy as elastic waves that propagate through the material, which can be detected, at a laboratory scale, by an array of AE sensors placed on the external surface of the specimen. The AE signals can be analysed to determine the location of microfractures caused by ice growth. To locate accurately AE events, the wave velocity field in the specimen must be known. A detailed explanation of AE methodologies is beyond the scope of this paper, and the sensor position design that we used to minimise uncertainties in the source location is given in Duca *et al.* (2014). In the following section, we briefly describe the experimental measurement of the velocity field and the localisation algorithm implemented. The procedure for AE data processing is detailed in Appendix 1.

Wave Velocity Models

Most algorithms employed to locate AE sources require as input the speed of propagation of the elastic waves. The velocity field in the specimen tested is inhomogeneous because of the vertical temperature profile. The P-wave velocity of the gneiss sample was measured by ultrasonic survey in order to examine changes in the material properties due to the thermal regime applied.
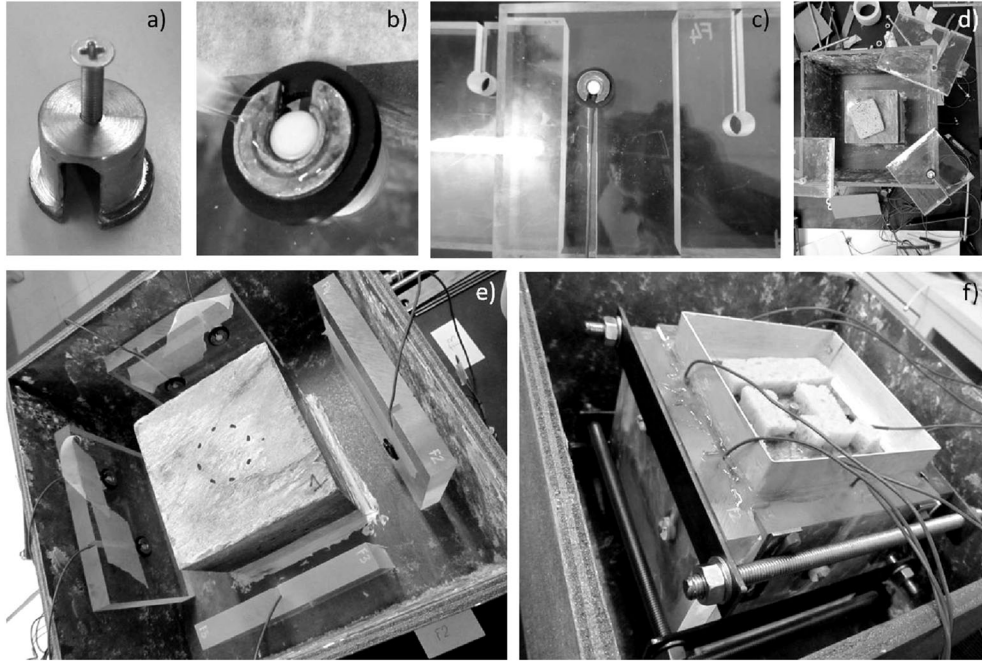
S. Duca *et al.*

Figure 3 Acoustic emission sensor installation: (a) sensor brass housing equipped with a stainless-steel screw to secure each sensor to the rock surface; (b) X60 two-component fast-curing adhesive to glue the brass housing on the rock surface; (c) plexiglass sheets with milled holes for the sensors; (d) the wooden box surrounding the sample, with a hole in the centre to allow placing of the sample directly on the cooling plate. Also shown is the building-up of the plexiglass cladding; (e) plexiglass sheets equipped with the sensors; (f) M12 screw bars to tighten the plexiglass against the sample and silicone sealing to prevent water loss.

A P-wave transmitter-receiver was placed on the top of the sample, perpendicular to the cleavage direction. The travel time of the P-waves was measured with a resolution of 1 µs; P-wave velocity was calculated by dividing the sample length by half the pulse transit time. Three series of measurements were performed on the sample: the first

when it was dry, the second when it was completely saturated and the third when it was frozen ($-12\,°C$). The ultrasonic velocities as a function of temperature and saturation are given in Table 2.

The ultrasonic velocity measured on the dry sample was about 1500 m/s, whereas the P-wave velocity obtained on the saturated sample was about 4300 m/s. The difference between them is consistent with data in Draebing and Krautblatter (2012). The penny-shape crack model (Nur and Simmons, 1969) must be applied in order to explain the significantly higher velocities in 'saturated' conditions compared to those in dry conditions. The P-wave velocity also increased significantly (14%) as a result of freezing, reaching 5500 m/s, consistent with data in Draebing and Krautblatter (2012).

Duca (2013) has hypothesised that the velocity variation within the sample depends on the state of water (frozen or unfrozen) in the pores and microcracks; this may be correlated with the ice-water saturation curve which characterises the frozen fringe and obtained by simulating an upward-freezing problem with the FEM code CODE_BRIGHT (Duca, 2013).

A simple layered velocity model is assumed (Figure 5), correlating the ultrasonic velocity with the thermal regime
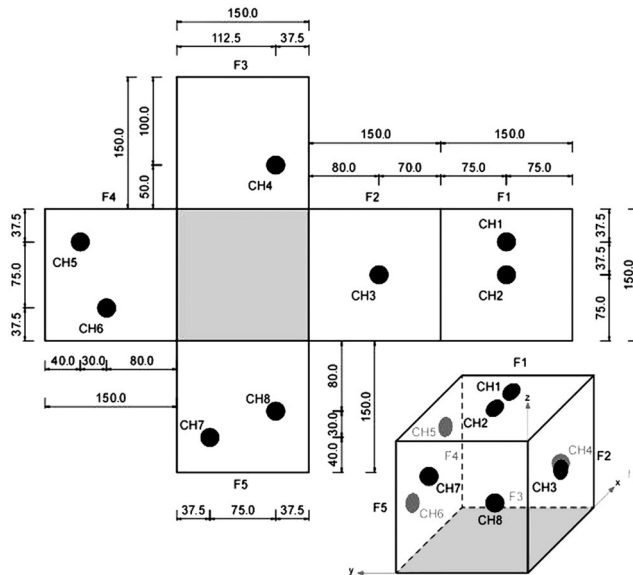

Figure 4 Optimal position of the eight acoustic emission sensors used in the experiment, represented on a flat cubic sample. units = mm; CH = channel; F = sample face.

Table 2 Ultrasonic measurements of the Arolla gneiss sample as a function of temperature and saturation.

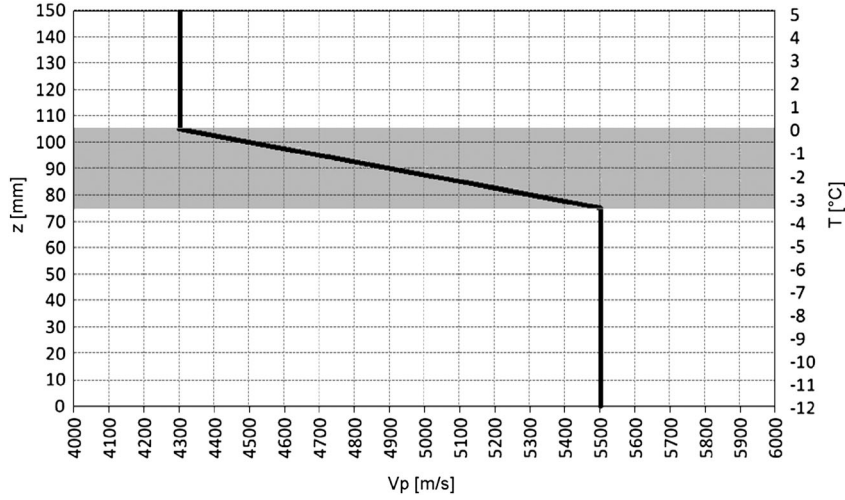|	Dry	Saturated (liquid)	Saturated (solid)
P-wave velocity	1582 m/s	4300 m/s	5500 m/s
Temperature	22 °C	22 °C	-12 °C

Figure 5 Horizontally layered velocity model: the grey band corresponds to the frozen fringe where wave velocity varies linearly as a function of the unfrozen water content curve. z = depth; Vp = P-wave velocity; T = temperature.
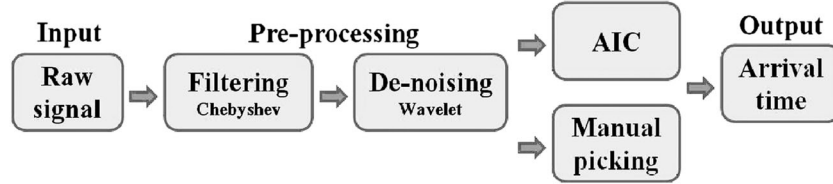

Figure 6 Block diagram of the semi-automated procedure to pick the first wave arrival time. AIC = Akaike Information Criterion.

in the sample and the resulting proportion of liquid water contained in the pores. The temperature regime in the sample simulated a thawed active layer above permafrost, and the temperature distribution determined the porewater phase:

- the upper layer was identified between the isotherms 5 °C (upper temperature boundary) and 0 °C (at 4.5 cm depth, assuming a linear temperature gradient). This layer was characterised by a P-wave velocity of 4300 m/s;
- the central layer (frozen fringe) was identified between the 0 °C and −3 °C isotherms. The P-wave velocity was assumed to vary linearly from 4300 m/s at 4.5 cm depth to 5500 m/s at 7.5 cm depth;
- the lower layer was characterised by a homogeneous velocity value (5500 m/s) because the temperature at the cold side of the frozen fringe was below −3 °C and the pore space was completely ice filled.

Table 3 Example of the pencil-break calibration test.

	X [mm]	Y [mm]	Z [mm]
Pencil lead source	85	112	150
Source (NLL)	88	113	147
Absolute error	3	1	3

Acoustic emission sources were localised using NonLinLoc (NLL) software and applying the layered velocity model.

Localisation Procedure

The basic principle of localisation procedures is to determine the source of an acoustic event starting from the wave velocity field and the arrival time of the stress waves of the surface of the monitored specimen. A key issue in AE localisation is a quick and accurate determination of the first arrival time from the recorded signals. Various methodologies have been described to determine the wave onset time (Baer and Kradolfer, 1987; Jurkewicz, 1988; Zhao and Takano, 1999; Anant and Dowla, 1997; Saragiotis *et al.*, 2002). Because of the abundant data recorded, an automated procedure was developed, mainly based on the use of wavelet decomposition (Shao *et al.*, 2011) and the Akaike Information Criterion (AIC) (Kitagawa and Akaike, 1978; Sarout *et al.*, 2009).

The AE data processing can be divided into four steps (Figure 6):

- raw signal filtering;
- de-noising by means of wavelet decomposition;
- arrival time estimation using AIC or manual picking;
- a posteriori signal classification based on the signal-to-noise ratio (SNR).

The source location was performed by means of a probabilistic, non-linear, global search methodology using the software NonLinLoc developed by Lomax (2000). The
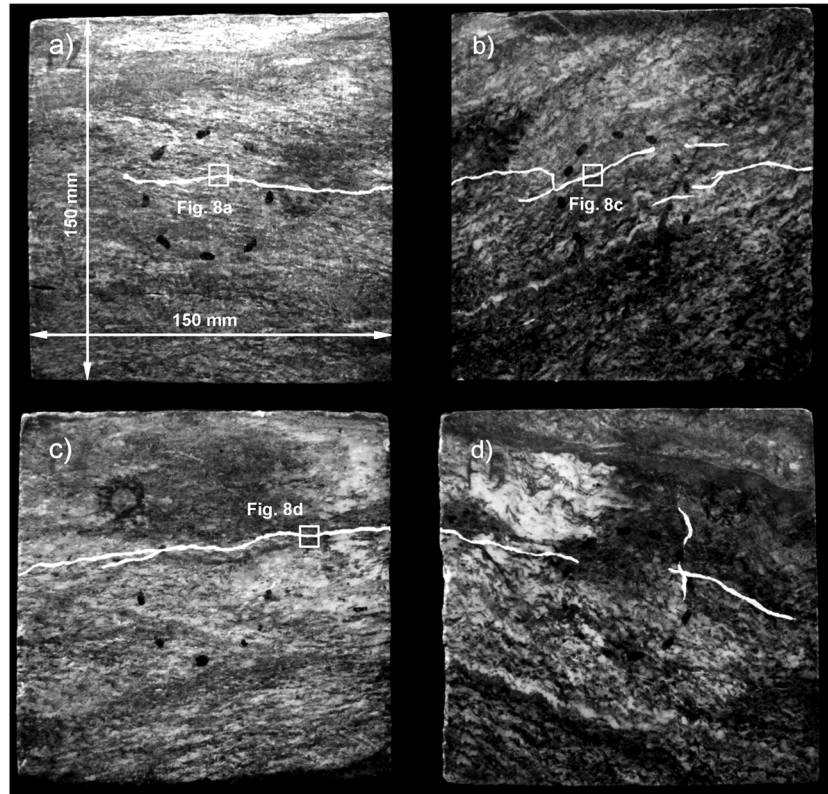
S. Duca *et al.*

Figure 7 (a–d) Pattern of superficial macrocracks marked on the four vertical sides of the sample; the cracks were traced with fluorescent paint and photographed after exposing the sample to Wood's lamp.
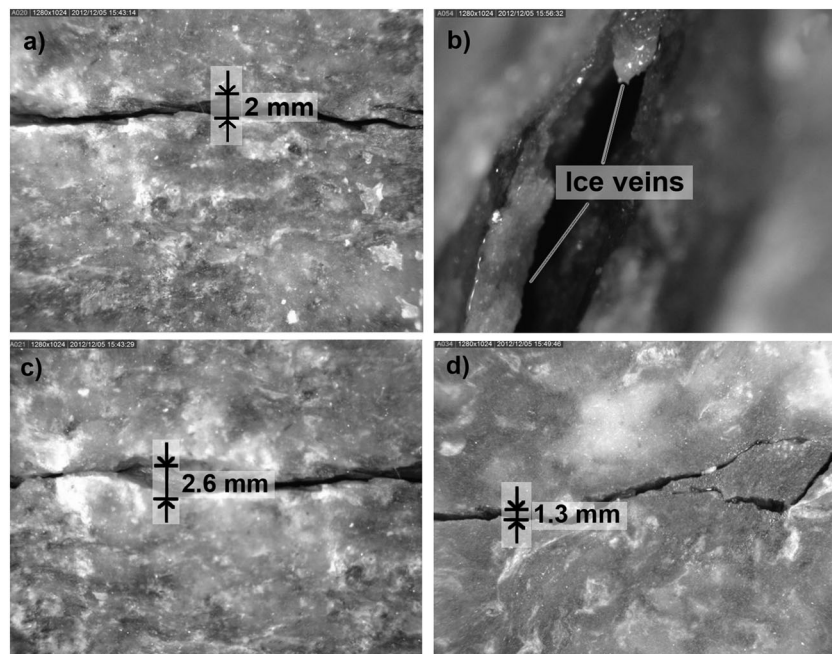

Figure 8 (a–d) Microphotographs showing details of the macrocracks on the specimen surfaces. See Figure 7 for locations.
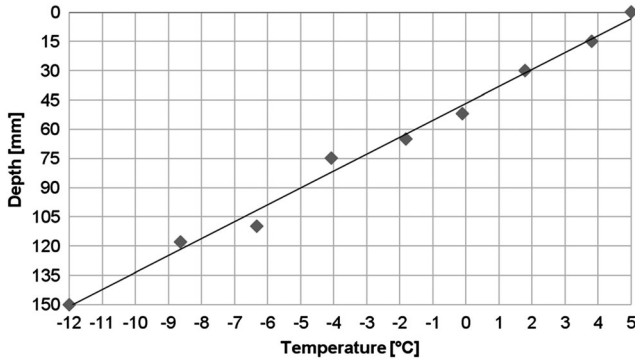
Figure 9   Temperature profile as a function of depth, maintained during 3 months of testing.

location algorithm used in NonLinLoc follows the inversion approach of Tarantola and Vallette (1982).

Pencil-Break Calibration Test

In order to configure and check the AE instrumentation and sensors, an accurate and reproducible means of generating AE signals at known positions is needed. A pencil-break test is commonly used for this purpose (Roberts and Talebzadeh, 2003): it helps to verify if the transducers have good acoustic contact with the monitored sample and check the accuracy of the source location algorithm. Applying the layered velocity models described in the previous paragraph, pencil-break-simulated sources must be localised: NonLinLoc software has been used (Table 3).

RESULTS

Fracture

At the end of 3 months of testing, the sample was cleaned to examine any weathering features produced during the experiment. Visual inspection of its surfaces revealed that microcracks had propagated horizontally through the gneiss, resulting in discontinuous and thick macrocracks near the base of the artificial active layer, partially filled with continuous veins of ice (Figures 7 and 8). The block had three distinct layers: its upper- and lower-thirds lacked visible cracks; the lower-third contained only pore ice; and the upper-third was water saturated. In contrast, the middle-third was fractured and rich in segregated ice: the fractures were at a depth between approximately 4.8 and 6.9 cm, corresponding to the frozen fringe.

Figure 8 shows microphotographs of fractures formed by ice segregation. In some cases, a filling of ice was visible inside the crack, despite melting of the ice close to the rock surface induced by sample cleaning. The ice was generally pure and white (bubble-rich), as shown in Figure 8b. Such bubbles are common in natural segregated ice (Murton *et al.*, 2000), and grow perpendicular to the direction of heat and water flow during ice segregation.

The measured profile of steady-state temperatures (reached after about 3 days of testing and maintained during the
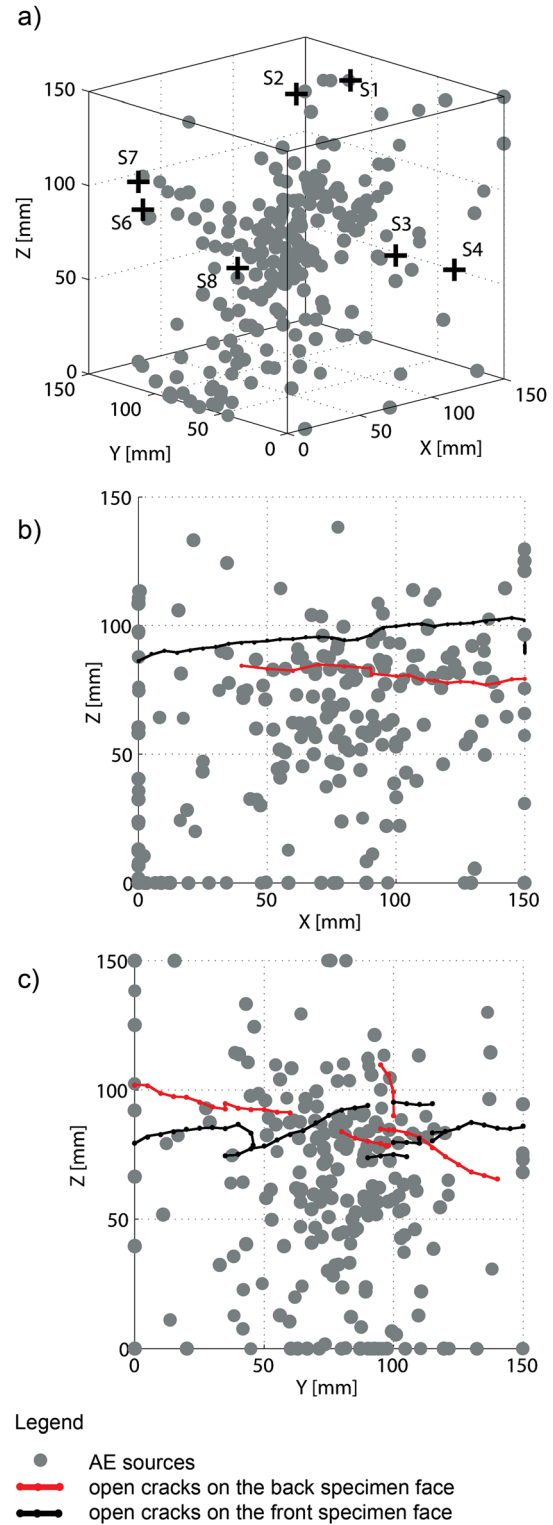

Figure 10   Hypocentre location of 227 acoustic emission (AE) high-quality events recorded during 3 months of testing: (a) 3D view of the AE sources localised using NonLinLoc software and applying a layered velocity model; black crosses indicate the position of the eight AE sensors; (b) and (c) lateral (X-Z) and (Y-Z) vertical views, respectively, indicating open crack patterns.
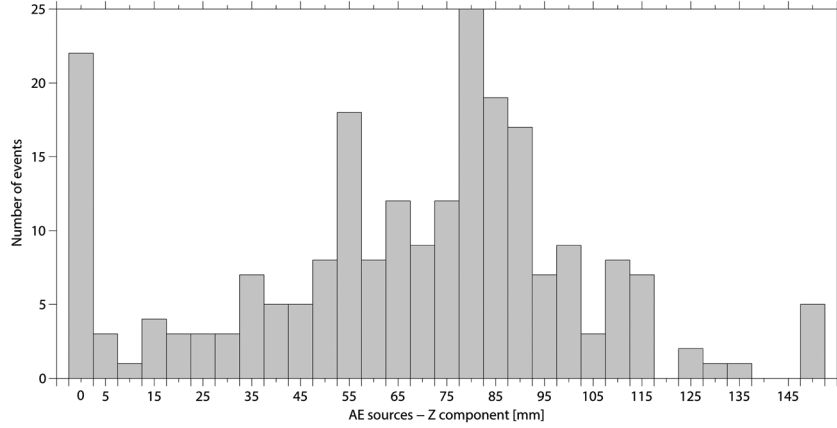
S. Duca *et al.*

Figure 11   Histogram showing the maximum acoustic emission (AE) activity concentrated at depths of 80–90 mm.
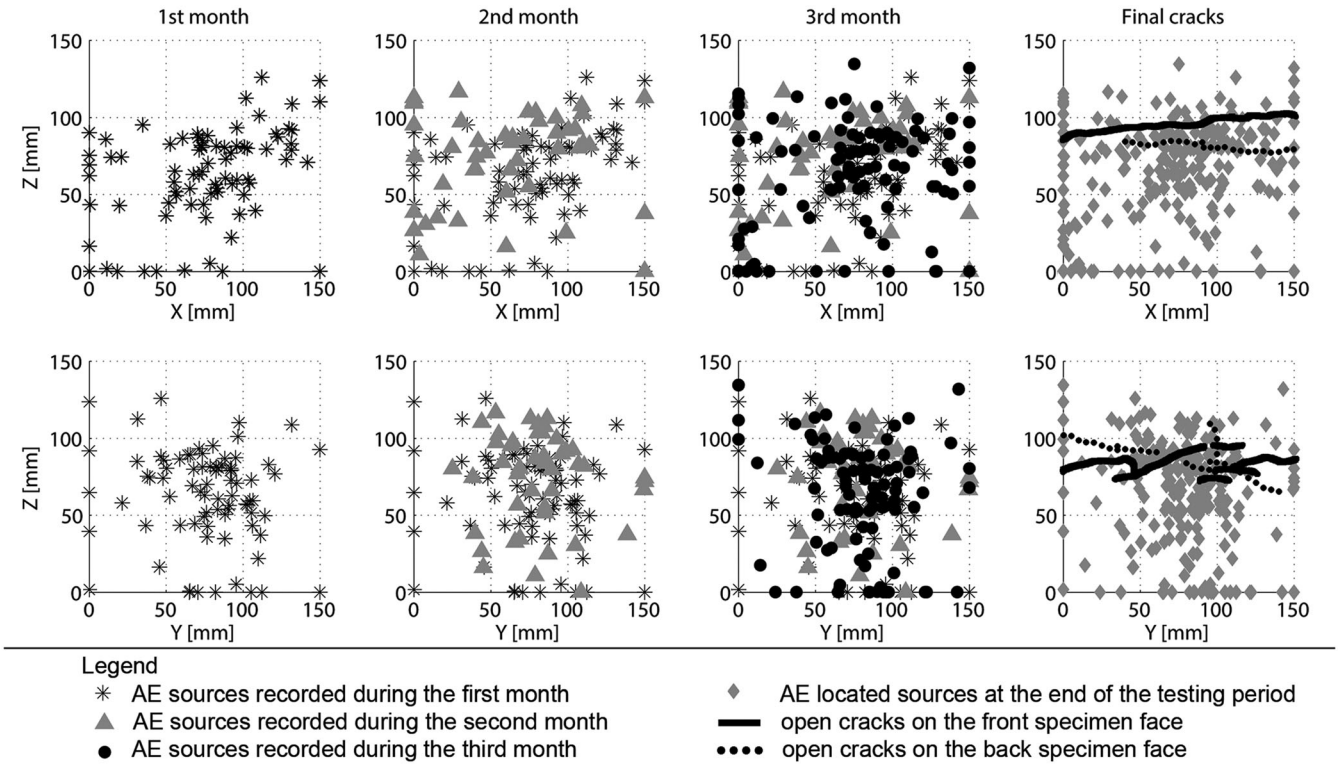

Figure 12   Temporal sequence and final source distribution of acoustic emission (AE) events on: first row, X-Z plane; second row, Y-Z plane.

experiment) is shown in Figure 9. The zero isotherm was located at a depth of 4.5 cm beneath the top of the block.

The fracture surfaces were rough and sub-parallel to the cooling surfaces. The average position of the crack zone corresponds to the −2 °C isotherm. The ice-lens growth was observed at positions in the block corresponding to a temperature range of −0.5 °C to −2.7 °C.

AE Source Location

A total of 729 AE events recorded during 3 months of testing were analysed using the procedure described in the previous paragraph. Only 227 AE events were characterised by SNR values > 10 dB. The seismic-phase arrival times for each high-quality signal were then used as input parameters in the NonLinLoc analysis, with a layered velocity model.

Figure 10 shows the hypocentre location of the 227 high-quality events recorded during 3 months of testing. AE sources were localised using NonLinLoc software and applying the layered velocity model described in the previous paragraph. The pattern of fractures detected at the end of the test is also plotted.
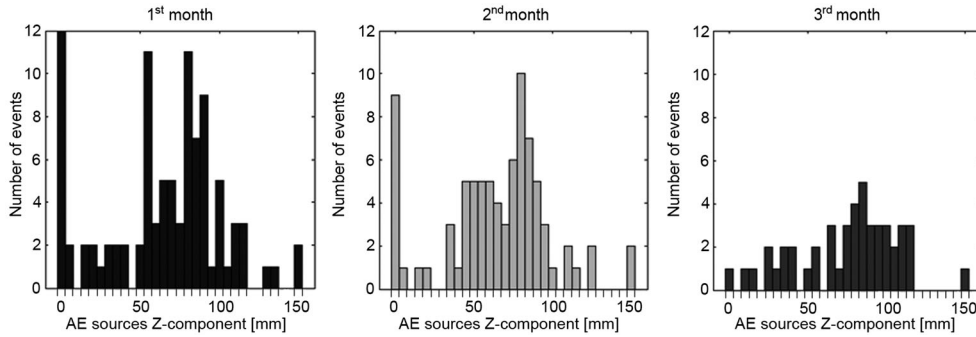
Figure 13 Histograms showing acoustic emission (AE) source Z-component distributions month by month.
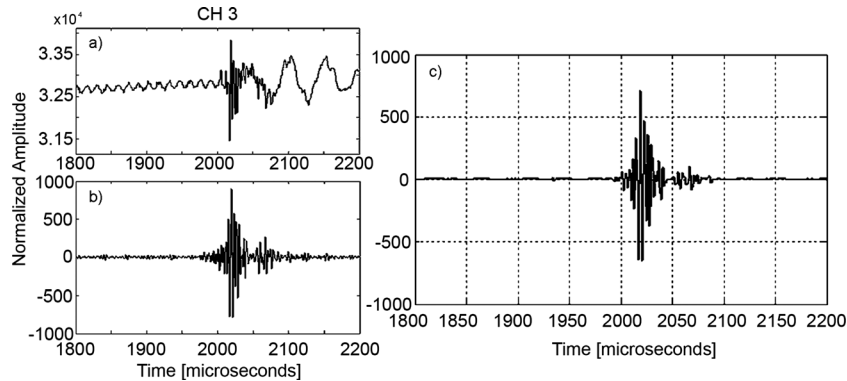

Figure 14 Signal recorded by channel 3 (CH 3) corresponding to an acoustic emission event on 22 February 2013: (a) raw signal; (b) filtered signal; (c) denoised signal.

The layered velocity model spreads the AE sources in the X and Y directions (in agreement with our experimental observations), and concentrates most of the AE activity in the central band in the Z direction. The source alignment to a particular depth can also be seen in the histogram in Figure 11: the maximum AE activity is concentrated in the depth range between 80 and 90 mm, in agreement with the fractures present at those depths.

In order to study the temporal sequence of AE events caused by ice growth during the laboratory test, hypocentres were plotted for each month (Figure 12). Histograms in Figure 13 show the AE source Z-component distributions month by month. During the first month, AE sources were scattered throughout the rock sample, probably because the ice formed during freezing-induced microcrack propagation, but the mechanism involved was due to volume expansion as water changed phase. During the second month, the hypocentres started to concentrate in the central part of the gneiss block, and in the last month, some AE sources were aligned along the macrocracks detected.

During the last month of testing, some recorded AE events were scattered throughout the block rather than concentrated in the central cracking band.

DISCUSSION AND CONCLUSIONS

In order to understand ice segregation and resulting crack growth in hard, intact rock, a downscaled physical simulation of this frost-weathering mechanism has successfully monitored microfracture development under a constant temperature gradient. A long-term freezing test performed on a fully saturated block of Arolla gneiss measuring $15 \times 15 \times 15$ cm used AEs to monitor microcracking induced by ice segregation. AE monitoring permits continuous, non-destructive determination of the approximate location of microfracture events and the rate of microcrack propagation caused by ice growth in rocks.

Hypocentres of recorded AE events were concentrated in a 40 mm thick band between 4.5 and 8 cm depth in the block. This layer approximately coincides with the frozen fringe, where unidirectional steady heat transfer and water transport induce fracture propagation by slow continuous freezing under a constant temperature gradient. Continued crack propagation resulted in the initiation of macrofractures visible on the outer surfaces of the block.

The temperature range of $-0.5\,°C$ to $-2.7\,°C$ within which ice lenses grew during the experiment is consistent with the theory of Walder and Hallet (1985). Although these authors proposed a temperature below $-5\,°C$ for ice segregation in hard, intact rocks with low porosity (e.g. granite), this value depends on the tensile strength of the rock: weaker rocks (tensile strength around 2 MPa) crack at temperatures closer to $0\,°C$. Considering the peculiarity of the thermally microcracked material tested, the rock temperature range for ice-lens growth essentially agrees with the Walder and Hallet (1985) model.

The scattering of some AE events throughout the block during the last month of the experiment may suggest that

S. Duca *et al.*

micro-cryosuction occurs in an area not precisely identifiable on the basis of theoretical isotherms (which should characterise the thermal regime of the sample), but in a wider area that reflects the inhomogeneity of the material. AE events outside of the frozen fringe may be of a thermo-mechanical nature, for example, thermal contraction cracks.

During this experiment many events induced by microfracture propagation have not been recorded, probably because they were below the sensitivity of the AE sensors.

Future work should determine the number of precisely localised events needed to allow the development of macrocracks. Upscaling of physical modelling experiments and monitoring of natural unweathered bedrock would provide valuable insights into permafrost landscape evolution and engineering geology.

APPENDIX 1

Because AE sensors commonly have an extremely high sensitivity, appropriate signal processing and noise reduction techniques are required in order to distinguish AE signals from noise. For the present work, we used a Chebyshev bandpass filter, with cutoff frequencies of 150–290 kHz: in this range the sensors used have the highest sensitivity. The filtered signals were de-noised further using a wavelet transform (WT) method (Sarout *et al.*, 2009). WT can be considered as a series of bandpass filters, whose results can be regarded as different mixtures of independent source signals (Shao *et al.*, 2011). WT provides a general transformation suitable to analyse transient signals (Sarout *et al.*, 2009) as a result of its ability to characterise the structure of the transient signal locally with a detail matched to its scale (by stretching or squeezing a given wavelet). The signals recorded during the experiment were filtered with Daubechies wavelet dB3 at level 4. Figure 14 shows an example of the signal-filtering process applied to the recorded events.

The AIC was used to estimate the arrival time. AIC belongs to a family of autoregressive methods (Sleeman and van Eck, 1999; Zhang *et al.*, 2003) based on statistical concepts (Sarout *et al.*, 2009). Kitagawa and Akaike (1978) showed statistically that a time series can be divided into two independent, and locally stationary, segments. For a given autoregressive process, the minimum point of the AIC function is the onset time separating the preceding noise from the actual arriving phase in a prescribed time window. The AIC method is effective for geophysical applications, both at field scale (Zhang *et al.*, 2003) and laboratory scale (Kurz *et al.*, 2005).

For a waveform $Vi(t)$ of length N, the AIC value at each sampling point j is defined as:

$$AIC(j) = j \log[\,\mathrm{var}(V_i[1,j])\,] \qquad (1)$$
$$+ (N - j - 1) \log[\,\mathrm{var}(V_i[j+1,N])\,]$$

where j ranges through all the waveform-sampling points, and var$(\cdot)$ denotes the variance of the signal data on the prescribed interval [1,j] or [j + 1,N]. The AIC picker defines the onset point as the global minimum. For this reason, it was necessary to choose a time window that includes only the waveform segments of interest (Sarout *et al.*, 2009): if the time window is chosen properly, the AIC picker is likely to determine accurately the arrival time of the phase sought.

In order to evaluate the signal 'quality', an a posteriori criterion based on the SNR was adopted. The SNR is defined as the amplitude ratio between a signal and the background noise, and it is normally evaluated using the equation:

$$SNR = 20 \log_{10}\left(\frac{A_{signal}}{A_{noise}}\right) \qquad (2)$$

where A is the root mean square amplitude.

The AE signals were classified according to the following criteria:

- good-quality signals, which have low background noise (SNR > 15 dB);
- medium-quality signals with an arrival time potentially distorted by noise (SNR in the range between 10 and 15 dB); and
- poor-quality signals, without any information (SNR < 10 dB).

Only those signals with SNR values greater than 10 were used to localise the AE sources in the experiment.

REFERENCES

Akagawa S, Fukuda M. 1991. Frost heave mechanism in welded tuff. *Permafrost and Periglacial Processes* **2**: 301–309. DOI: 10.1002/ppp.3430020405.

Anant SK, Dowla FU. 1997. Wavelet transform methods for phase identification in three-component seismogram. *Bulletin of the Seismological Society of America* **87**: 1598–1612.

Baer M, Kradolfer U. 1987. An automatic phase picker for local and teleseismic events. *Bulletin of Seismological Society of America* **77**: 1437–1445.

Chen TC, Yeung MR, Mori N. 2003. Effect of water saturation on deterioration of welded tuff due to freeze-thaw action. *Cold Regions Science and Technology* **38**: 127–136.

Draebing D, Krautblatter M. 2012. P-wave velocity changes in freezing hard low-porosity rocks: a laboratory-based time-average model. *The Cryosphere Discussions* **6**: 793–819.

Duca S. 2013. Design of an experimental procedure and set up for the detection of ice segregation phenomena in rock by acoustic emissions. PhD thesis, Politecnico di Torino, Italy.

Duca S, Occhiena C, Sambuelli L. 2014. A procedure to determine the optimal sensor positions for locating AE sources in rock samples. *Rock Mechanics and Rock Engineering*. DOI: 10.1007/s00603-014-0582-0

Hallet B, Walder JS, Stubbs CW. 1991. Weathering by segregation ice growth in microcracks at sustained subzero temperatures: Verification from an experimental

study using acoustic emissions. *Permafrost and Periglacial Processes* **2**: 283–300. DOI: 10.1002/ppp.3430020404.

Jurkewicz A. 1988. Polarization analysis of three-component array data. *Bulletin of Seismological Society of America* **78**(5): 1725–1743.

King MS, Pettitt WS, Haycox JR, Young RP. 2011. Acoustic emissions associated with the formation of fracture sets in sandstone under polyaxial stress conditions. *Geophysical Prospecting* **60**(1): 93–102.

Kitagawa G, Akaike H. 1978. A procedure for the modeling of non- stationary time series. *Annals of the Institute of Statistical Mathematics* **30**: 351–363.

Kurz JH, Grosse CU, Reinhardt HW. 2005. Strategies for reliable automatic onset time picking of acoustic emissions and of ultrasound signals in concrete. *Ultrasonics* **43**: 538–546.

Lomax A, Virieux J, Volant P, Berge C. 2000. Probabilistic earthquake location in 3D and layered models: Introduction of a Metropolis-Gibbs method and comparison with linear locations. In Advances in Seismic Event Location, Thurber CH, Rabinowitz N (eds). Kluwer: Amsterdam; 101–134.

Matsuoka N. 1990. Mechanisms of Rock Breakdown by Frost Action - an Experimental Approach. *Cold Regions Science and Technology* **17**: 253–270. DOI: 10.1002/ppp.620.

Matsuoka N, Murton J. 2008. Frost weathering: recent advances and future directions. *Permafrost and Periglacial Processes* **19**: 195–210.

Miller RD. 1978. Frost heaving in non-colloidal soils. In Proceedings of the 3rd International Conference on Permafrost.

Edmonton, Alberta, Canada. Washington D.C., National Academy Press **1**: 707–713.

Murton JB, Coutard JP, Lautridou JP, Ozouf JC, Robinson DA, Williams RBG, Guillemet G, Simmons P. 2000. Experimental design for a pilot study on bedrock weathering near the permafrost table. *Earth Surface Processes and Landforms* **25**: 1281–1294.

Murton JB, Coutard JP, Lautridou JP, Ozouf JC, Robinson DA, Williams RBG. 2001. Physical modeling of bedrock brecciation by ice segregation in permafrost. *Permafrost and Periglacial Processes* **12**: 255–266. DOI: 10.1002/ppp.390.

Murton JB, Peterson R, Ozouf JC. 2006. Bedrock Fracture by Ice Segregation in Cold Regions. *Science* **314**(5802): 1127–1129.

Nishimura S, Gens A, Olivella S, Jardine RJ. 2009. THM-coupled finite element analysis of frozen soil: formulation and application. *Geotechnique* **59**(3): 159–171.

Nur A, Simmons G. 1969. The effect of saturation on velocity in low porosity rocks. *Earth and Planetary Science Letters* **7**: 183–193.

Ondrasina L, Kirchner D, Siegesmund S. 2002. Freeze-thaw cycles and their influence on marble deterioration: a long-term experiment. *Geological Society of London Special Publications* **205**: 9–18.

Roberts TM, Talebzadeh M. 2003. Acoustic emission monitoring of fatigue crack propagation. *Journal of Constructional Steel Research* **59**: 695–712.

Saad A, Guedon S, Martineau F. 2010. Microstructural weathering of sedimentary rocks by freeze-thaw cycles. Experimental study of state and transfer parameters. *Comptes Rendus Geoscience* **342**: 197–203.

Saragiotis CD, Hadjileontiadis LJ, Panas SM. 2002. PAI-S/K: A robust automatic seismic P-phase arrival identification scheme. *IEEE*

Transactions on Geoscience and Remote Sensing **40**: 1395–1404.

Sarout J, Ferjani M, Guéguen Y. 2009. A semi-automatic processing technique for elastic-wave laboratory data. *Ultrasonics* **49**: 452–458.

Shao H, Shi X, Li L. 2011. Power signal separation in milling process based on wavelet transform and independent component analysis. *International Journal of Machine Tools & Manufacture* **51**: 701–710.

Sleeman R, van Eck T. 1999. Robust automatic P-phase picking: an on-line implementation in the analysis of broadband seismogram recordings. *Physics of the Earth and Planetary Interiors* **113**: 265–275.

Tarantola A, Vallette B. 1982. Inverse problems = quest for information. *Journal of Geophysical Research* **50**: 159–170.

Walder JS, Hallet B. 1985. A theoretical model of the fracture of rock due to freezing. *Geological Society of America Bulletin* **96**(3): 336–346.

Whalley WB, Bruce BR, Rainey MM. 2004. Weathering, blockfields, and fracture systems and the implications of long-term landscape formation: some evidence from Lingen and Oksforddjokelen areas in North Norway. *Polar Geography* **28**: 93–119.

Zhang H, Thurber C, Rowe C. 2003. Automatic p-wave detection and picking with multiscale wavelet analysis for single-component recordings. *Bulletin of the Seismological Society of America* **93**(5): 1904–1912.

Zhao Y, Takano K. 1999. An artificial neural network approach for broadband seismic phase picking. *Bulletin of the Seismological Society of America* **89**: 670–680.